Earth and Planetary Science Letters 552 (2020) 116596

Contents lists available at ScienceDirect

Earth and Planetary Science Letters

www.elsevier.com/locate/epsl

Taking the pulse of volcanic eruptions using plagioclase glomerocrysts

Anders McCarthy [a,*], Cyril Chelle-Michou [b], Jonathan D. Blundy [a,c], Pierre Vonlanthen [d], Anders Meibom [e,f], Stéphane Escrig [e]

[a] School of Earth Sciences, Wills Memorial Building, University of Bristol, UK
[b] Department of Earth Sciences, ETH Zürich, Switzerland
[c] Department of Earth Sciences, University of Oxford, UK
[d] Institut des Science de la Terre, University of Lausanne, Switzerland
[e] Laboratory for Biological Geochemistry, School of Architecture, Civil and Environmental Engineering, Ecole Polytechnique Fédérale de Lausanne, Switzerland
[f] Center for Advanced Surface Analysis, Institute of Earth Sciences, University of Lausanne, Switzerland

ARTICLE INFO

Article history:
Received 29 February 2020
Received in revised form 15 September 2020
Accepted 18 September 2020
Available online xxxx
Editor: H. Handley

Keywords:
Tolbachik volcano
plagioclase glomerocryst
rapid crystal growth
volatile-fluxing
nano-SIMS
orbicules and comb layering

ABSTRACT

Crystallization timescales in subvolcanic systems and the consequences of interaction between ascending magmas and gases remain largely unconstrained, as do links between these processes and monitoring signals at restless volcanoes. We apply diffusion chronometry to radially-oriented plagioclase and associated olivine in a glomerocryst from Tolbachik volcano (Kamchatka, Russia) to elucidate such processes. We show that cm-size glomerocrysts grow in a few days prior to, or during, eruption. Melt inclusions from these glomerocrysts show no compositional evolution during crystallization, implying growth in a melt-rich and dynamic environment. Volatile elements in melt inclusions show significant variability, with increasing CO_2 as H_2O decreases. This behaviour is inconsistent with normal degassing processes, and more likely reflects CO_2-fluxing. On the basis of short residence timescales of glomerocrysts and sharp changes in melt inclusion volatile abundances, we propose that rapid (pre-)eruptive crystallization is controlled by rhythmic fluxing of magmatic H_2O and CO_2 through the sub-volcanic conduit. This implies that compositional zoning in plagioclase, from resorption textures to oscillatory zoning, record short-term CO_2- and H_2O-fluxing episodes, consistent with strombolian eruption dynamics. We propose that volcanic glomerocrysts represent the counterpart of vertical igneous layering (or comb layering) in shallow plutons. Magmatic layering and glomerocrysts dominated by radial plagioclase offer novel ways of targeting short-term crystallization and degassing processes in subvolcanic systems.

1. Introduction

Volcanic eruptions are controlled by two fundamental processes: advection of fresh batches of hot magma from deep reservoirs towards the surface (e.g. Sparks et al., 1977; Bouvet de Maisonneuve et al., 2013); and degassing of dissolved volatiles (CO_2, H_2O, SO_2) from magmas during ascent (Woods and Cardoso, 1997). Magmatic H_2O is a key component controlling the stability of different mineral assemblages and crystallization dynamics during their emplacement in the crust (e.g. Feig et al., 2006; Annen et al., 2006). Magmatic CO_2, on the other hand, has only recently become the focus of attention, as illustrated by the elevated CO_2 abundances in melt inclusions in a variety of geodynamic settings (Métrich et al., 2010; Blundy et al., 2010; Caricchi et al., 2018).

The low solubility of CO_2 in magmas compared to H_2O (Newman and Lowenstern, 2002; Papale, 2005; Ghiorso and Gualda, 2015) implies that ascending CO_2-rich fluids exsolve from deep reservoirs and interact with H_2O-rich shallower magmatic systems (Papale 2005; Blundy et al., 2010; Yoshimura, 2015; Caricchi et al., 2018). A consequence of the low solubility of CO_2 compared to H_2O is that a small addition of CO_2 to H_2O-saturated magmas can have a significant effect on the confining pressures of magmatic reservoirs (Blundy et al., 2010; Caricchi et al., 2018). Ascent of volatiles through arc crust is thought to occur on short (hourly-monthly) timescales and is well recorded by intra-crustal earthquake swarms (Chouet, 1996; Shapiro et al., 2017) and volcanic gas emissions. However, long-lived magmatic systems tend to erase petrological evidence of such events. Thus, finding petrological evidence in fossil volcanic and plutonic environments for

* Corresponding author.
E-mail address: anders.mccarthy@bristol.ac.uk (A. McCarthy).

https://doi.org/10.1016/j.epsl.2020.116596

such transient magmatic processes is instrumental to better constrain the conditions leading up to, and accompanying, volcanic eruptions.

Tolbachik volcano, Kamchatka, Russia, was the site of the Great Fissure Eruption (GTFE) of 1975-1976, one of the largest basaltic eruptions of the 20th century (Fedotov et al., 1980a,b; Punin et al., 2010; Churikova et al., 2015). During the initial months of the GTFE, extensive strombolian activity formed four large scoria cones southwest of Plosky Tolbachik (55.832°N, 160.326°S) (Fedotov et al., 1980a). Explosive eruptions of scoria, ash, bombs and gas-rich pyroclastic clouds occurred rhythmically (period of 0.5–1 seconds, Fedotov et al., 1980a). Explosive activity of scoria cones continued during subsequent effusive-style eruptions from multiple fissures (Fedotov et al., 1980a). Eruption of cruciform and spherical crystal-lapilli (or glomerocrysts) were recorded during the initial stages of explosive, strombolian activity of the GTFE which led to the formation of large scoria cones (Fedotov et al., 1980a; Punin et al., 2010) (Fig. 1).

We employed diffusion chronometry of Sr in plagioclase and P in olivine to retrieve residence timescales, as well as major-, trace- and volatile analysis of melt inclusions. We show that these radial glomerocrysts result from rapid crystal growth as a consequence of decompression-driven crystallization in shallow conduits on volcanic timescales. We argue that resorption and growth of plagioclase are controlled by pre- to syn-eruptive rhythmic CO_2- and H_2O-fluxing and discuss possible consequences regarding plagioclase zoning and igneous layering in shallow plutons.

2. Methods

A representative 3 cm-wide plagioclase glomerocryst was impregnated with epoxy resin and cut into two equal hemispheric parts using a wire saw. The surface of interest was then polished stepwise down to 1 µm diamond paste, and carbon coated. Panchromatic cathodoluminescence (CL) images were taken at the University of Lausanne, using a CamScan MV2300 SEM operated at 20 kV and ~10 nA. Because of the large size of the sample, scanning was carried out on a mosaic grid of several hundred fields, and reconstructed using AutoPano Giga® 4.2.3 software. CL imaging allowed us to constrain the zoning patterns in a constituent crystal of the glomerocryst using imaging processing software (Fig. 1 and electronic appendix Figs. S1, S2).

Analyses of major elements in plagioclase (electronic appendix Fig. S2) and olivine were acquired on a JEOL 8200 SuperProbe at the Institute of Earth Sciences, University of Lausanne. Analytical conditions were 15 kV, 15 nA, and 1 µm beam size. Counting times were 30 s on the peak and 15 s on the background on either side of the peak. Natural silicates were used as standards. Step size of profiles was 10 µm. Additional analysis of plagioclase at higher spatial resolution prior to SIMS analysis were carried out using the JEOL JXA8530F HyperProbe FEG-EPMA at the School of Earth Sciences, University of Bristol, with analytical conditions 15 kV, 15 nA and <1 µm beam size and 1 µm step size.

High-resolution profiles of ^{7}Li, ^{23}Na, ^{26}Mg, ^{27}Al, ^{28}Si, ^{39}K, ^{40}Ca, ^{49}Ti, ^{88}Sr, ^{138}Ba in plagioclase were acquired on Au-coated polished mounts by secondary ion mass spectrometry (SIMS) at the NERC ion-microprobe facility, University of Edinburgh, using a Cameca IMS-4f instrument. Prior to acquisition, a pre-sputtering raster along the length of the profile with a nominal 10 kV primary beam of O^- ions and 10 nA beam was applied. Analyses were then performed with a 0.02 nA beam current to achieve a ~1 µm diameter spot at the sample surface.

Melt (glass) rimming the plagioclase crystals, and as inclusions and embayments in olivine and plagioclase was analysed using the Cameca SX100 EPMA of the School of Earth Sciences, University of Bristol. Analytical conditions were 20 kV, 4 nA, 5 µm beam size; Na and K were measured first. Standards were silicates, oxides and metals (Fig. 2).

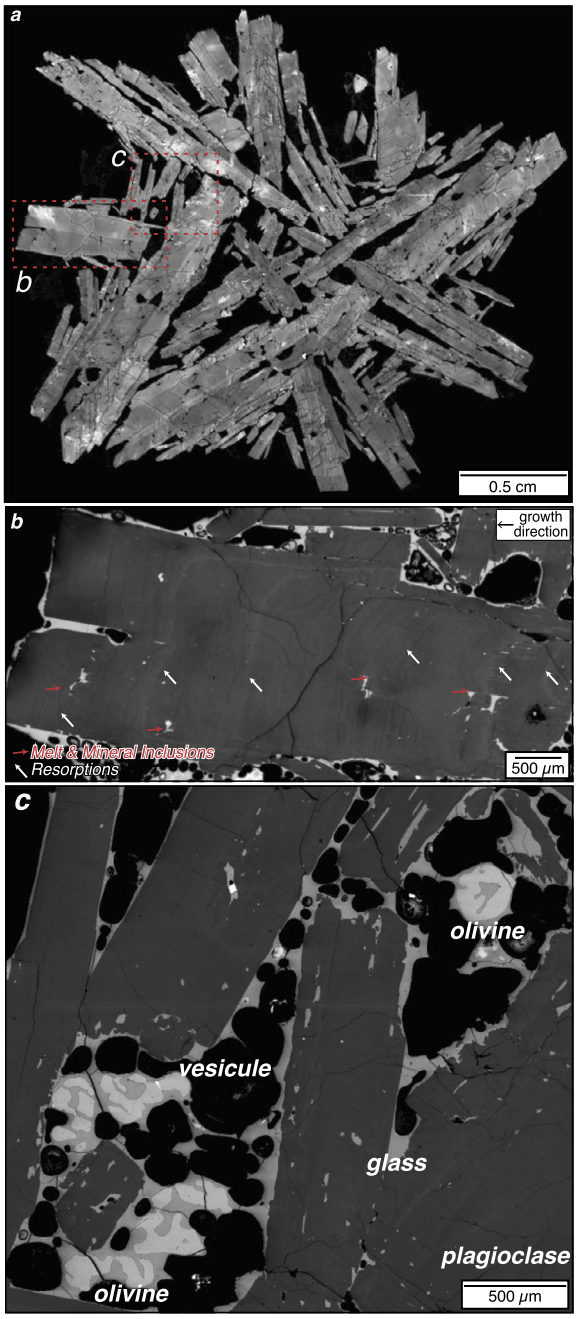

Fig. 1. (a) Panchromatic cathodoluminescence (CL) of a radially-oriented plagioclase glomerocryst from Tolbachik volcano; (b) Close up SEM image of a plagioclase crystal with oscillatory zoning, resorption textures followed by higher-Anorthite plagioclase (white arrows), and local inclusions of melt, olivine or oxides (red arrows); (c) Close-up of anhedral olivine crystals (light grey) with melt inclusions and embayments in between plagioclase crystals in the glomerocryst. (For interpretation of the colours in the figure(s), the reader is referred to the web version of this article.)

Trace elements and H_2O contents of matrix glass and melt inclusions (electronic appendix Fig. S3) in plagioclase and olivine were acquired on Au-coated polished mounts by secondary ion mass spectrometry (SIMS) at the NERC ion-microprobe facility, University of Edinburgh, using a Cameca IMS-4f instrument. Analyses were performed with a nominal 10 kV primary beam of O^- ions and 5 nA beam current focused to a ~10-15 µm diameter spot at the sample surface. A small raster was applied prior to acquisition to limit charging. H_2O was measured as $^{1}H^+$ secondary ions

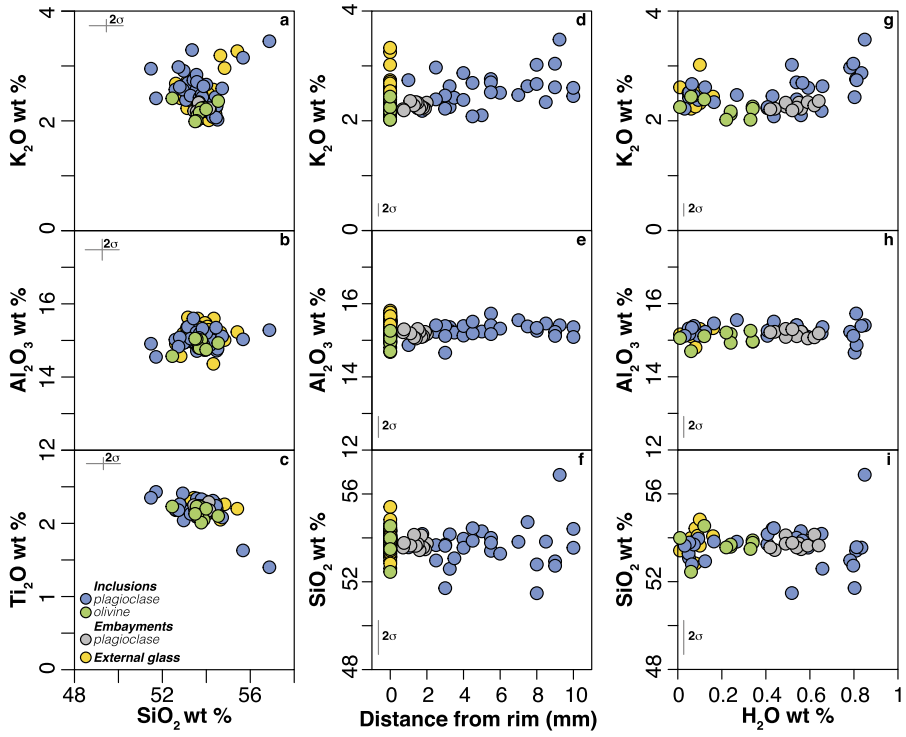

Fig. 2. Major elements composition of melt inclusions in plagioclase and olivine, glass in plagioclase embayments, and external glass rimming the glomerocryst; a–c) K_2O, Al_2O_3 and TiO_2 wt% versus SiO_2 wt%; d-f) K_2O, Al_2O_3 and SiO_2 wt% versus glomerocryst rim-core distance (0 = rim of the plagioclase); g-i) K_2O, Al_2O_3 and SiO_2 wt% versus H_2O wt%. (errors are 2σ). Some compositional variation such as higher SiO_2 in occasional melt inclusions nearer the core of the glomerocryst are not unexpected as shown by the compositional variation of erupted tephra and lavas that occurred during the formation of scoria cones during the GTFE (Fedotov et al., 1980a).

at a nominal mass resolving power (M/ΔM) of 300 and 25 µm image field. Trace elements were analysed simultaneously with $^{1}H^{+}$. For H_2O, calibration involved a working curve of $^{1}H/^{30}Si$ versus H_2O ($r^2 > 0.99$) based on glasses of known H_2O concentration (0–2.82 wt%). Analytical uncertainty of H_2O for each analysis is between 0.55–7.50%, 2σ.

CO_2 contents of glasses are very low and require special sample preparation and analytical approaches. A section of the plagioclase glomerocryst was mounted in indium (to reduce background), cleaned with acetone and ethanol and gold-coated. CO_2 in melt inclusions was analysed by SIMS using a Cameca 7f-GEO ion-probe at Caltech (California, USA). A 10 keV Cs^{+} primary ion beam of ~4-5 nA (~15 µm in diameter) was used to sputter the samples and produce secondary ions. Negative secondary ions of 9 keV were collected with Faraday cups ($^{16}O^{-}$ and $^{28}Si^{-}$) or an electron multiplier (EM, for $^{12}C^{-}$) in peak-jumping mode. The energy bandwidth for the secondary ions was ~45 eV. A mass resolving power (MRP) of ~5000 was used to separate $^{16}OH^{-}$ from $^{17}O^{-}$. A field aperture was utilized to limit secondary ion signals to the centre ~10 µm of the crater. Any possible edge effect was further eliminated with a 36% (in area) electronic gating. Ion images of $^{12}C^{-}$ and $^{16}OH^{-}$ were examined on each spot to avoid possible contaminations from tiny holes or cracks on the samples. Each measurement consisted of 120 s pre-sputtering and 20 cycles of data collection, with counting times of 2 s for $^{12}C^{-}$ and 1 s for all other ions ($^{16}O^{-}$, $^{16}OH^{-}$, ^{28}Si) in each cycle. Data were corrected for detector backgrounds and EM deadtime. The CO_2 background of the instrument was checked with a San Carlos olivine grain or the Suprasil 3002 glass (~0.2 ppm CO_2). Two in-house basaltic glass standards (WOK5-4, 64 ppm; WOK16-2, 184 ppm) were used to calibrate CO_2 concentrations. Replicate analysis of one melt inclusion gave values of 39.2 and 40.8 ppm, within the analytical uncertainty of each analysis (±2 ppm, 2σ).

Wavelength-dispersive spectroscopy (WDS) X-ray mapping of P in olivine was carried out at the School of Earth Sciences, University of Bristol, using a Cameca SX100 electron probe microanalyzer (EPMA) operated at 20 kV and 200 nA, with 1 µm beam and step size, and a dwell time of 0.15 ms. Phosphorus was measured on all five spectrometers and counts were accumulated to enhance signal/background ratios (electronic appendix Fig. S4). In addition, high spatial resolution profiles of P were acquired using the JEOL JXA8530F HyperProbe operated between 7-10 kV and 20-100 nA, with a <1 µm beam size. Phosphorus was standardized on Durango apatite; olivine MongOL Sh11-2 was analysed (nominal 66 ± 20 ppm P; Batanova et al., 2019) as an internal standard prior to measuring profiles, giving a value of 94 ppm (±7 ppm) for P at 100 kV and 100 nA. Measurements were performed on four spectrometers with counts cumulated and counting times of 60 s or 120 s (electronic appendix Fig. S4).

Profiles of P in olivine were acquired by nano-SIMS using the Cameca N50L of the Ecole Polytechnique Fédérale in Lausanne, (electronic appendix Fig. S4). Samples were previously coated with a 10-15 nm gold layer to prevent the build-up of charge on the sample surface. A Cs^{+} primary beam was used to sputter the olivine and the ion species $^{16}O^{-}$, $^{28}Si^{-}$, $^{31}P^{-}$, $^{24}Mg^{16}O^{-}$ were extracted and measured at the same time using electron multipliers, at mass resolution sufficient to resolve any potential mass-interferences. The location of the line-scans was selected to be perpendicular to the zonation previously identified using WDS X-ray maps of P. A pre-sputtering phase was performed on a 30 × 30 µm area of interest at a larger beam size (diaphragm D1-2, 4.5 pA for the Cs^{+} primary beam) with a dwell time of 1 ms/pixel. This was followed by a line scan of 2 cycles to clean up the profile of interest with beam conditions of D1-3 and 2 s/pixel. Acquisition of high-resolution line scans was performed using a finer beam. These include longer profiles (D1-3, ca. 150 nm beam diameter, 2 pA Cs^{+} beam, 20 scans with 2 s/pixel) as well as shorter profiles (D1.5, 80 nm beam diameter, 0.1 pA Cs^{+} beam, 45 scans with 2 s/pixel). $^{24}Mg^{16}O^{-}$ was monitored for possible variations in the ionization and extraction processes as it is expected to be

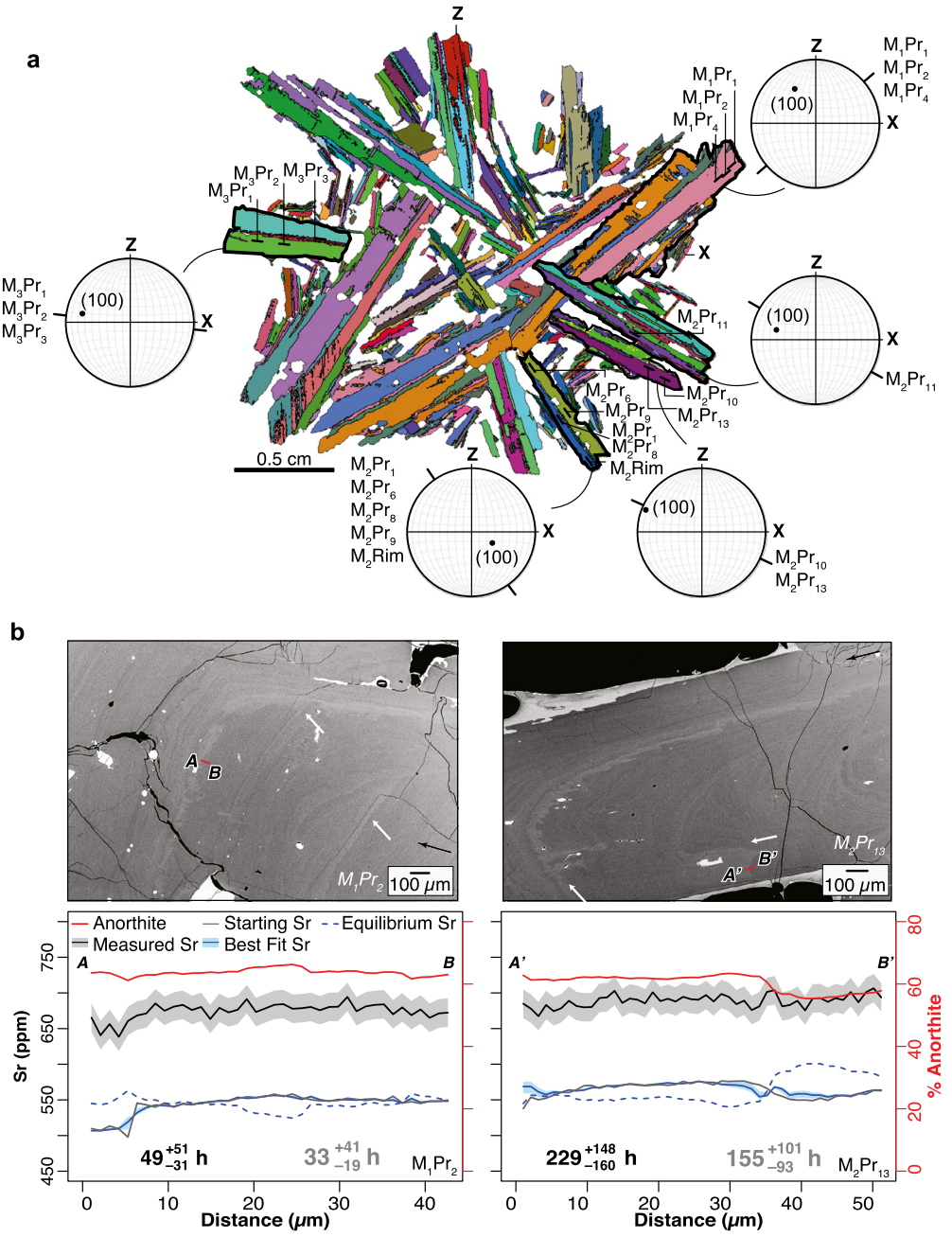

Fig. 3. (a) All-Euler Electron Back-Scatter Diffraction (EBSD) map and (100) pole figures for the plagioclase glomerocryst, together with the traces of Sr profiles measured by SIMS. Note that (010) twins belonging to the same grain (coded with different colours as they have different Euler angle triplets) have identical orientations of (100) poles. Pole figures in a and b are represented on lower hemisphere equal area projections; (b) Two representative BSE images and SIMS profiles of Sr (and anorthite), with diffusion timescales calculated at 1100 °C and 1075 °C for two profiles from the Tolbachik glomerocryst. All measured Sr and anorthite profiles and calculated Sr-diffusion timescales can be found in the electronic appendix. The dashed line shows the equilibrium Sr profile based on the measured An profile, calculated following Dohmen and Blundy (2014). The limited diffusion of measured Sr towards the equilibrium profile is indicative of short timescales.

homogenous in the olivine measured. In order to minimize potential instrumental drift, we normalize profiles to $^{28}Si^{-}$, based on EPMA analysis of olivine and chemical mapping. As the spatial resolution of nano-SIMS is higher than FEG-EPMA (electronic appendix Fig. S5), the residence timescales based on modelling diffusion profiles of P in olivine have been calculated exclusively from the nano-SIMS profiles.

Crystallographic orientation of olivine and plagioclase was determined by electron backscatter diffraction (EBSD) at the Institute of Earth Sciences, University of Lausanne, using a Tescan Mira II LMU FEG-SEM equipped with the Symmetry EBSD detector and the Aztec® 3.4 software package (Fig. 3a and electronic appendix Fig. S4). Analyses were done at 20 kV and 1.1 nA, on a sample tilted at 70° with respect to the horizontal. As EBSD requires a pristine crystal lattice up to the sample surface, additional surface finish using colloidal silica suspension was used to remove any mechanical damage induced by diamond polishing. No carbon coating was applied to ensure optimal EBSD pattern quality. Olivine ([100] = 4.756 Å, [010] = 10.207 Å, [001] = 5.980 Å, $\alpha = 90.0°$, $\beta = 90.0°$, $\gamma = 90.0°$) and plagioclase ([100] = 8.194 Å, [010] = 12.897 Å, [001] = 14.190 Å, $\alpha = 93.0°$, $\beta = 115.8°$, $\gamma = 91.2°$) reference files from the HKL and American Mineralogist databases, respectively, were used for indexing. Points of analysis were characterized by three Euler angles ($\varphi 1, \Phi, \varphi 2$) which could be compiled into pole

figures to display the orientation of the crystal axes with respect to a sample reference frame.

3. Results

CL (Fig. 1) and EBSD (Fig. 3a) mapping indicate that plagioclase glomerocrysts are formed of radially-oriented, twinned plagioclase crystals growing from a central part of the glomerocryst towards the exterior, similar to experimental work on glomerocrysts by Arzilli et al. (2015). Sections of micron-wide oscillatory zoning in plagioclase (Fig. 1 and electronic appendix Figs. S1, S2) are rhythmically interspersed with resorption zones (Figs. 1, 3b). Plagioclase crystals vary in composition between An_{55}–An_{65}, with occasional sharp increase to An_{70} along resorption zones (Fig. 1 and Fig. S2). The textural and compositional characteristics are consistent with previous observations of Tolbachik plagioclase glomerocrysts from the GTFE (Punin et al., 2010). Plagioclase crystals have abundant melt, olivine and oxide inclusions, and are coated by quench glass with no evidence of (micro)-phenocrysts, implying rapid cooling upon eruption (Fig. 1b, c). Olivine is found as small grains in plagioclase or as larger (ca. 500 microns) anhedral grains with abundant melt inclusions and melt embayments (Fig. 1c). These larger olivine grains occur at the outer rims and at the centre of the glomerocryst between elongated plagioclase crystals (Fig. 1). Olivine is unzoned in major elements ($Fo_{71.6}$ to $Fo_{73.6}$) but shows well-defined phosphorous zoning patterns. Basaltic-andesitic melt inclusions in plagioclase and olivine as well as the external glass coating the minerals are overall homogenous in major and trace element compositions (Fig. 2 and electronic appendix Fig. S3). One inclusion from the internal part of the glomerocryst has an andesitic composition and lower TiO_2 concentration (Fig. 2). The variation in melt inclusions resembles more differentiated tephra erupted during the formation of scoria cones of the GTFE (e.g. Fedotov et al., 1980a). Such exceptions aside, melt inclusion chemistry remains almost constant, for both compatible and incompatible elements (e.g. Al_2O_3, K_2O Fig. 2, Zr, Ba, La/Ce, electronic appendix Fig. S3) across the entire suite and shows no correlation with H_2O abundances or distance from the core to the rim of the glomerocryst (Fig. 2). This observation indicates that there has been very little (if any) post-entrapment crystallisation of melt inclusions. Moreover, the similarity of melt inclusions and matrix glasses indicates that the melt composition in the system as whole changed little during glomerocryst crystallisation. This observation has implications for the size of the system in which the glomerocrysts grew (see below).

CO_2 abundances in most glass inclusions in plagioclase remain low (<80 ppm), except for one inclusion at 1200 ppm. CO_2 abundances show an inverse correlation with H_2O with H_2O decreasing by ca. 0.3 wt% as CO_2 increases by ca. 50-60 ppm (see discussion). It is possible that post-entrapment volatile loss could occur, leading to low-H_2O abundances at constant CO_2 concentrations. Although we cannot discount post-entrapment modification, this is unlikely for several reasons. Quenched glass coating the glomerocrysts is consistent with their eruption as crystal-lapilli during Strombolian activity of the GTFE (Fedotov et al., 1980a; Punin et al., 2010) rather than in basaltic lava flows, thus implying rapid cooling upon eruption. We also note that glass inclusions and embayments in olivine show generally lower H_2O abundances than plagioclase glass inclusions, consistent with their growth shortly upon – or during – eruption at low H_2O abundances and after the growth of plagioclase at higher H_2O activity (see discussion). Moreover, the systematic increase in CO_2 abundances with decreasing H_2O is inconsistent with simple post-entrapment dehydration or rehydration that should occur at constant CO_2.

4. Numerical modelling

Magma temperatures: The temperature of the melt was estimated using the major element chemistry and H_2O abundances of glass inclusions in plagioclase (Dataset S3) with the model of Sisson and Grove (1993). Average calculated temperatures are 1083 ± 26 °C (2SD). Note that one SiO_2-rich glass inclusion yielded a lower temperature at 1030 °C. Considering the uncertainty on the temperature, diffusion timescales in olivine and plagioclase have been computed at 1100 °C and 1075 °C.

Sr diffusion in plagioclase: The initial Sr profiles in plagioclase were computed using known plagioclase/melt partition coefficients ($Kp_{(Sr)}$; Dohmen and Blundy, 2014) which is a function of melt composition (CaO = 7.19 ± 0.98 wt% (2σ), measured on plagioclase-hosted glass inclusions), plagioclase composition (X_{An}) and temperature (1100–1075 °C). An Sr melt concentration of 247 ± 15 ppm (2σ) measured on plagioclase-hosted melt inclusions was used.

The diffusion coefficients of Sr in plagioclase depend on both temperature and chemical composition (Cherniak and Watson, 1994; Giletti and Casserly, 1994). More specifically, most experimental datasets report a constant activation energy on the order of 265 kJ/mol, whereas the pre-exponential factor, $\log(D_0)$, varies linearly with the molar proportion of anorthite (X_{An}).

We have compiled the Sr diffusion in plagioclase measurements of Cherniak and Watson (1994) and Giletti and Casserly (1994). A multiple linear regression of the 97 diffusion measurements (T = 550–1300 °C; X_{An} = 0.01–0.96) yields the following parameters for the Arrhenius equation (fitting parameter uncertainties given at 1σ):

$$D_{Sr} = 10^{-5.2(\pm 0.4)-3.3(\pm 0.1)\cdot XAn} \cdot \exp \frac{-264\,(\pm 8)}{RT} \quad (1)$$

with a residual standard error of 0.4 log units on 94 degrees of freedom (electronic appendix Fig. S6).

Diffusion anisotropy of Sr in $An_{60\text{-}70}$ plagioclase has been shown experimentally to be minimal, with values either falling within experimental uncertainty (Giletti and Casserly, 1994) for all crystallographic orientations, or peaking at ~0.7 log units (Cherniak and Watson, 1994) for diffusion normal to the (010) and (001) planes, respectively. Whenever possible and for the sake of consistency, plagioclase grains were selected so that (100) poles were oriented within the same plane as the Sr profile traces (Fig. 3a), although no explicit correction for crystallographic orientation was made.

Strontium diffusion in plagioclase was modelled at 1100 °C and 1075 °C, using a finite difference scheme according to Costa et al. (2008) and Dohmen et al. (2017). In order to improve model stability on regions of steep anorthite gradient, we used a half grid between the normal grid spaces (Dohmen et al., 2017). The thermodynamic parameter for Sr (A_{Sr}) representing the non-ideal interaction of Sr with the major components of plagioclase (anorthite and albite) was computed according to Dohmen and Blundy (2014). Time steps (Δt) and space steps (Δx) were of 1 h and 1 µm, respectively, to ensure that the Courant condition was fulfilled for each grid points at all time ($\frac{D\cdot\Delta t}{(\Delta t)^2} < 0.5$; mostly <0.03). For each profile Sr diffusion was modelled using the computed initial Sr profile as described above and two types of boundary conditions: (i) no flux at the boundary (closed system) with $[Sr]_1^{all\ time} = [Sr]_2^{all\ time}$ and $[Sr]_n^{all\ time} = [Sr]_{n-1}^{all\ time}$; or (ii) exchange at the boundary with a reservoir of constant Sr content, $[Sr]_1^{all\ time} = [Sr]_1^{initial}$ and $[Sr]_n^{all\ time} = [Sr]_n^{initial}$ (open system) (Fig. 3b, Table 1 and electronic appendix Figs. S7, S8, S9, S10).

The accuracy of the partitioning model of Dohmen and Blundy (2014) was estimated on the order of 50% relative; the precision

Table 1
Calculated residence timescales (in hours) of nine plagioclase profiles at 1100 °C and 1075 °C. Quoted uncertainties include analytical uncertainty of the Sr measurement (±20 ppm, 2σ) propagated onto the diffusion time with a Monte Carlo method by generating 1000 starting profiles for each measured profile and assuming a normal error distribution. All the results given in hours at 95% confidence level. All profiles can be found in the electronic appendix.

1100 °C	M_1Pr_1	M_1Pr_2	M_2Rim	M_2Pr_1	M_2Pr_8	M_2Pr_9	M_2Pr_{10}	M_2Pr_{13}	M_2Pr_{11}
Closed system	40^{+134}_{-33}	33^{+41}_{-19}	6^{+34}_{-5}	25^{+28}_{-19}	25^{+49}_{-24}	31^{+211}_{-29}	72^{+118}_{-67}	155^{+101}_{-93}	114^{+133}_{-112}
Open system	39^{+176}_{-32}	38^{+192}_{-24}	8^{+43}_{-7}	30^{+45}_{-23}	21^{+35}_{-17}	18^{+102}_{-17}	73^{+151}_{-71}	343^{+294}_{-200}	102^{+125}_{-101}
1075 °C	M_1Pr_1	M_1Pr_2	M_2Rim	M_2Pr_1	M_2Pr_8	M_2Pr_9	M_2Pr_{10}	M_2Pr_{13}	M_2Pr_{11}
Closed system	60^{+176}_{-51}	49^{+51}_{-31}	6^{+61}_{-5}	37^{+38}_{-29}	35^{+81}_{-34}	50^{+322}_{-48}	99^{+173}_{-95}	229^{+148}_{-160}	172^{+206}_{-167}
Open system	58^{+278}_{-49}	57^{+449}_{-39}	12^{+78}_{-11}	44^{+67}_{-36}	30^{+64}_{-24}	26^{+124}_{-25}	96^{+229}_{-96}	494^{+413}_{-299}	151^{+183}_{-150}

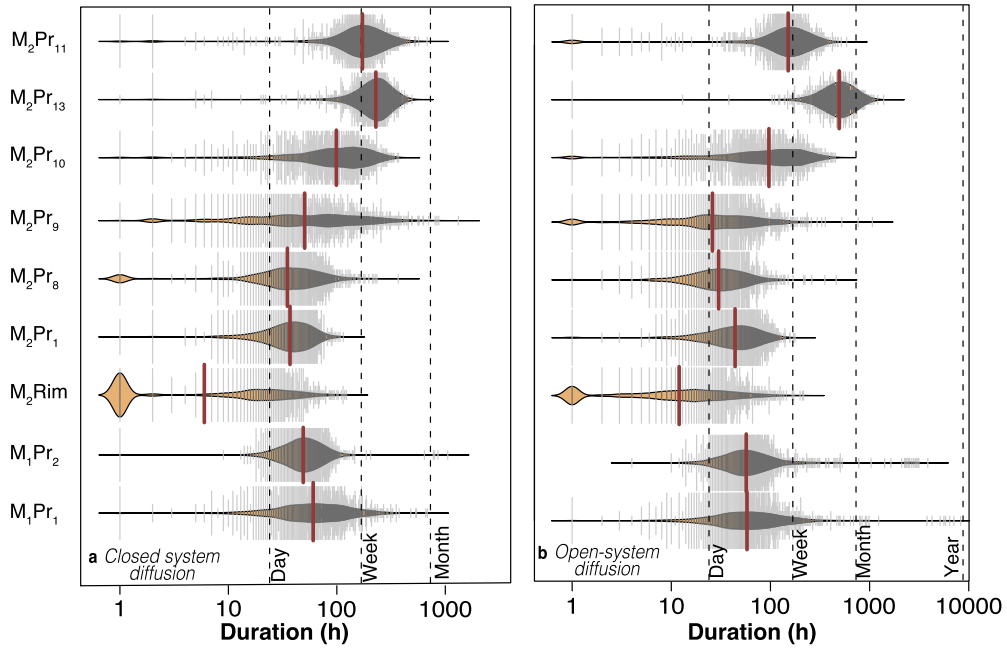

Fig. 4. Violin plots summarizing the calculated Sr diffusion timescales in plagioclase for a total of nine profiles (closed and open system) at 1075 °C. See Table 1 and supplementary materials for timescales at 1100 °C. This probabilistic representation results from the propagation of the analytical uncertainty of the Sr measurement (±20 ppm, 2σ) onto the diffusion time with a Monte Carlo method by generating 1000 starting profiles for each measured profile and assuming a normal error distribution (see methods section for further details). Bold red bars represent the median diffusion timescale of the 1000 Monte Carlo replicas (grey bars). Note that the timescale of the plagioclase rim (M2_Rim) overlaps with that of late-stage olivine (Fig. 5).

of the method, based on normal error propagation of the relevant fit parameters in Dohmen and Blundy (2014), is considerably better, ∼3% relative. Therefore, while the absolute partition coefficient and computed initial Sr concentration in plagioclase may differ by 50% from the true value, the relative internal variation of the starting profile is considerably less. Thus, in order to compare the measured and computed diffusion profiles we normalized each profile to its mean value. Diffusion times were estimated by root-mean-square error minimization of the normalized measured and computed diffusion Sr profiles. Analytical uncertainty of the Sr measurement (±20 ppm, 2σ) was propagated onto the diffusion time with the Monte Carlo method by generating 1000 starting profiles for each measured one and assuming a normal error distribution. For each of the 1000 generated profiles (per measured profile), a diffusion time could be estimated (by root mean-square error minimization), allowing us to estimate the uncertainties. We report the results at 95% confidence (Table 1). We calculated precise timescales for 9 out of 14 SIMS profiles, with five other profiles showing similar values but larger uncertainties as a result of smaller variations in plagioclase anorthite and Sr abundances (electronic appendix Figs. S7, S8, S9, S10). The calculated timescales are as short as 6 h for the plagioclase rim and vary between 35 and 230 h for profiles in plagioclase interiors (Table 1, Figs. 3b, 4). As expected, from crystal interior to crystal rim, Sr diffusion profiles in plagioclase record increasingly shorter durations (e.g., see M_2Pr_1, M_2Pr_8 and M_2Rim) (Figs. 3, 4), confirming the suitability of our modelling approach. This also allows us to estimate crystal growth rates. The distance between these profiles is ca. 0.3 cm (M_2Pr_1, M_2Pr_8 and M_2Rim, Fig. 3a), corresponding to an average time interval of ca. 18–30 h (closed and open system, Table 1), suggesting an average growth rate ranging between $2.7 \cdot 10^{-6}$ and $4.6 \cdot 10^{-6}$ cm/s.

Phosphorous-diffusion in olivine: seven nano-SIMS $^{31}P/^{28}Si$ profiles were fitted to an error function by nonlinear weighted least-squares regression using a Levenberg-Marquardt type fitting algorithm (Fig. 5 and Figs. S4, S5). Weighting uncertainties were estimated using the standard deviation of the flat parts of the signal (on both sides of the step) and propagated linearly to each point as a function of the count ratio intensity. Experimentally-derived diffusion coefficients (Watson et al., 2015) at T° of 1100 °C and 1075 °C (see next paragraph) were applied (Table 2). Uncertainties on the fitted diffusion profiles and durations are given at 2σ; they correspond to regression uncertainties only and do not account for uncertainties of the P diffusion coefficient. Diffusion anisotropy of P in olivine is within experimental error (Watson et al., 2015) and, therefore, is not considered in the calculations. Cal-

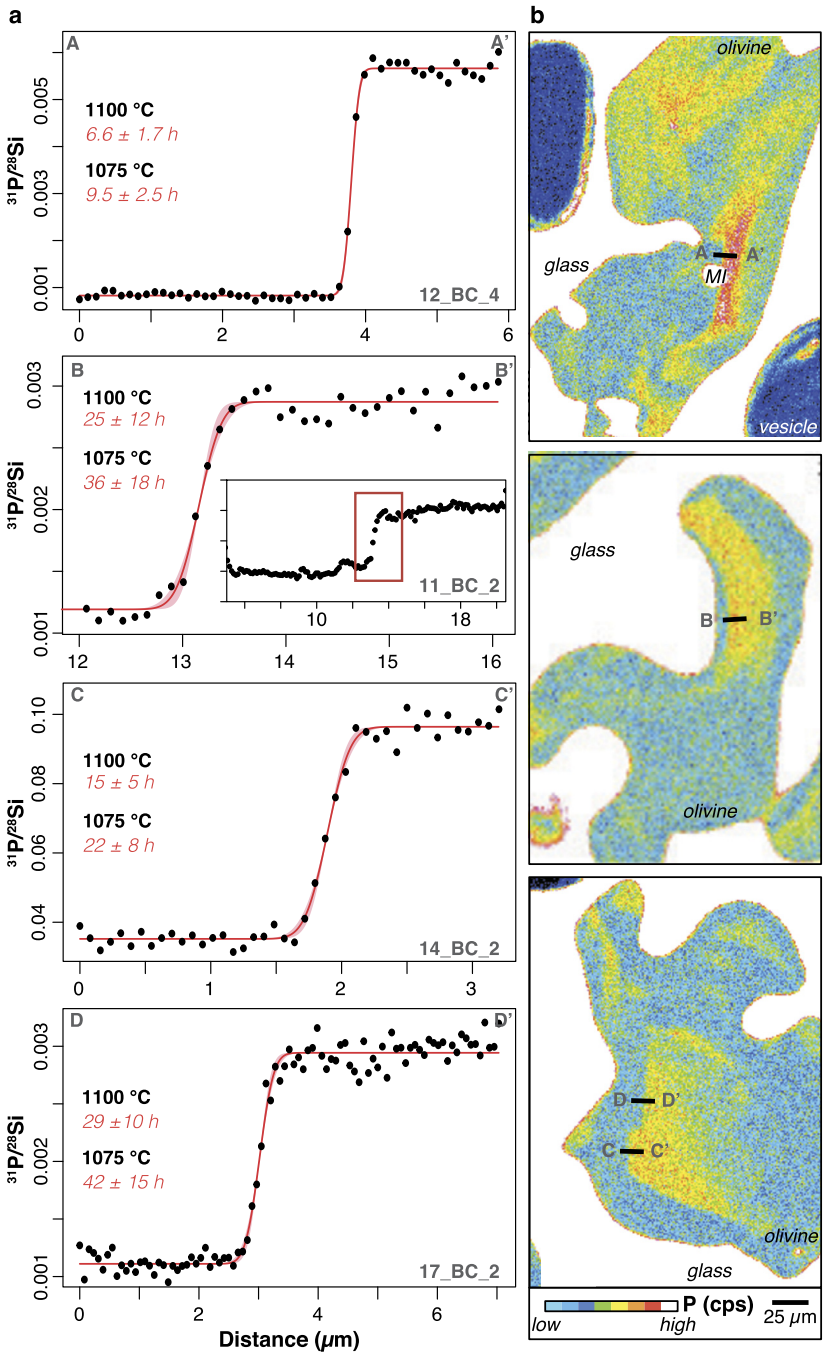

Fig. 5. (a) Measured Nano-SIMS Phosphorous compositions in olivine (black dots), together with the diffusion profiles calculated for temperatures of 1100 °C and 1075 °C (red line); (b) WDS X-ray maps of P in anhedral olivine with location of the Nano-SIMS profiles shown in a. MI = melt inclusion. EBSD pattern of the olivine can be found in the electronic appendix.

Table 2
Calculated residence timescales of seven olivine profiles (in hours) based on phosphorous diffusion as a function of different temperatures (in °C). All profiles can be found in the electronic appendix.

	10_BC_2	11_BC_2	12_BC_4	14_BC_2	15_BC_2	17_BC_2	20_PBC_10
1100 °C	129 ± 11	25 ± 12	6.6 ± 1.7	15 ± 5	89 ± 16	29 ± 10	130 ± 34
1075 °C	187 ± 16	36 ± 18	9.5 ± 2.5	22 ± 8	129 ± 23	42 ± 15	188 ± 49

culated timescales vary between 130 and 6.6 h at 1100 °C, and 188 and 9.5 h at 1075 °C (Table 2). The shortest timescales based on P-diffusion in olivine are less than most timescales estimated for Sr-diffusion in plagioclase interiors, but overlap with calculated timescales for the plagioclase rim (Table 1).

Rhyolite-MELTS modelling: The starting composition of Rhyolite-MELTS modelling was based on the average glass composition of glass inclusions in plagioclase, with conditions of QFM+1, consistent with moderately oxidized magmas found at Tolbachik (Kamenetsky et al., 2017). Variations in CO_2 and H_2O abundances

were set to cover the range of volatile abundances measured in glass inclusions, with saturation in different proportions of volatiles calculated using MagmaSat (Ghiorso and Gualda, 2015). The initial temperature stability of plagioclase at different CO_2-H_2O conditions (1150-1063 °C) calculated using Rhyolite-MELTS overlaps the temperature estimates using Sisson and Grove (1993) and measured temperatures for lava flows from the southern cone during the GTFE (1030–1070 °C, Fedotov et al., 1980a).

Thus, our objective is to evaluate the effect of changing H_2O and CO_2 on the stability and composition of plagioclase and highlighting mechanisms leading to the growth of radial glomerocrysts on short timescales.

5. Discussion

5.1. Glomerocrysts record daily to weekly magmatic timescales

Glomerocrysts are frequently interpreted as remobilized fragments of pre-cursor crystal mush (Cashman et al., 2017) implying relatively long pre-eruptive residence times in hot intracrustal systems. Shallow magmatic systems, however, are prone to conditions that promote disequilibrium crystallization, namely rapid crystal growth as a result of abrupt changes in magmatic undercooling, occasioned by shifts in pressure, temperature, or volatile concentration (Blundy and Cashman, 2005; McCarthy and Müntener, 2016). Unlike blocky, euhedral plagioclase indicating near-equilibrium crystallization at low undercooling, Tolbachik glomerocrysts comprise 1.5 cm-long radiating plagioclase crystals (Figs. 1, 3). Such textures have been shown experimentally to result from rapid, disequilibrium crystallisation (e.g. Lofgren and Donaldson, 1975; Arzilli et al., 2015). This is consistent with the well-developed twinning of each elongated plagioclase crystal (Fig. 3a), which results from elevated anisotropy in crystal growth rates leading to radiating plagioclase glomerocrysts (Punin et al., 2010). Olivine associated with these glomerocrysts is anhedral and shows well-defined, sharp P zoning patterns (Fig. 1c). The anhedral habit of olivine with subangular to rounded rims and the presence of abundant embayments and melt inclusions is further evidence of rapid-growth (e.g. Mourey and Shea, 2019). Such conditions of rapid crystal growth are consistent with the well-defined phosphorous zoning in these olivine grains, a characteristic likely arising because of the low diffusivity of phosphorous in the melt (Fig. 4b) (e.g. Milman-Barris et al., 2008).

Calculated timescales from Sr diffusion in plagioclase at 1075 to 1100 °C yield hourly to weekly residence timescales (Table 1, Figs. 3 and 4). Timescales for olivine based on phosphorous-diffusion are as short as 6–42 h (Table 2, Fig. 5). The overlap between olivine and plagioclase rim timescales is consistent with textural observations indicating that olivine crystallizes after initiation of plagioclase growth, likely a consequence of decompression-driven crystallization (e.g. McCarthy and Müntener, 2016) (*see below*).

Volatile abundances in melt inclusions show a maximum estimated saturation pressure of 200 MPa (Fig. 6b). Assuming a residence time of a week, based on the residence timescale of these plagioclase crystals (Table 1), this implies minimum steady ascent rates on the order of ~30 MPa/day. Experimentally-determined growth rates of texturally similar, near-liquidus alkali feldspar glomerocrysts peak at 1.4 to $2.4 \cdot 10^{-6}$ cm/s (Arzilli et al., 2015), whereas plagioclase crystallized from decompression experiments between 10–200 MPa on basaltic-andesites reach lower growth rates of $2.9 \cdot 10^{-7}$ cm/s (Shea and Hammer, 2013). The characteristic radial texture of these glomerocrysts likely reflects heterogeneous nucleation as a consequence of a prior event of superheating of the melt which has led to the resorption of pre-existing minerals and nuclei (e.g. Arzilli et al., 2015). Under such conditions,

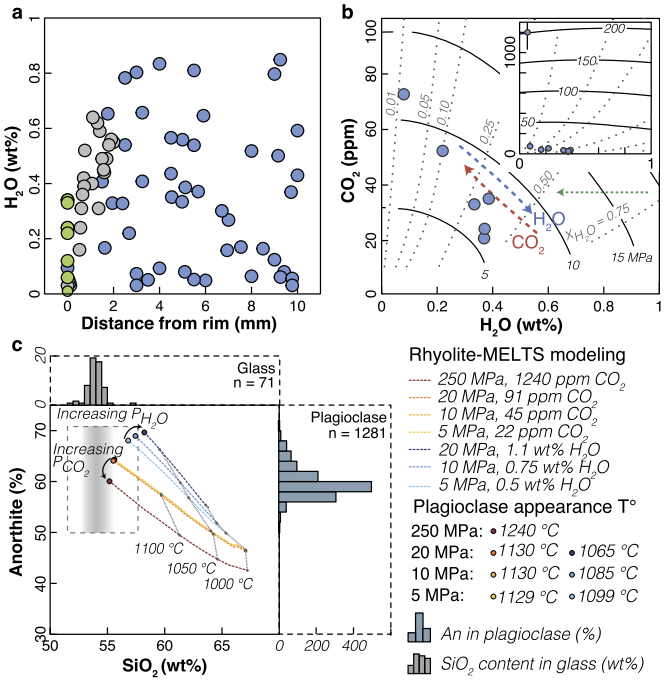

Fig. 6. (a) H_2O abundance in melt inclusions and embayments in a plagioclase glomerocryst as a function of distance from the rim of the host crystals; (b) CO_2 (ppm) vs H_2O (wt.%) of the same melt inclusions. Inset shows a melt inclusion with surprisingly elevated CO_2 (1200 ppm) at low H_2O (<800 ppm) within the central part of the plagioclase glomerocryst. The analytical standard deviations (2σ) for H_2O and CO_2 generally lie within the symbol size. Vapour isopleths and isobars (MPa) are calculated using MagmaSat at FMQ+1 log unit for the average composition of Tolbachik melt inclusions; (c) Rhyolite-MELTS modelling of plagioclase anorthite content as a function of SiO_2 and CO_2-H_2O abundances; Note the histogram of plagioclase anorthite composition of the Tolbachik glomerocryst (light-blue histogram) and melt composition (grey histogram). In (c), H_2O-loss in the melt as a result of CO_2-fluxing will lead to a shift in plagioclase composition as well as an increase in the upper temperature stability of plagioclase. The red and blue arrows indicate the effect of CO_2- and H_2O-fluxing, respectively, whereas the green arrow represents a shift to lower H_2O without a concomitant decrease in CO_2 as a consequence of disequilibrium degassing (Pichavant et al., 2013; Yoshimura, 2015) or post-entrapment diffusive H_2O loss.

mineral growth is favoured over nucleation, leading to the formation of radially-oriented mineral aggregates at elevated growth rates (Arzilli et al., 2015) very similar to our estimated growth rates. Thus, growth rates of plagioclases forming glomerocrysts are likely to be on the order of 10^{-6} cm/s (Arzilli et al., 2015). Such elevated growth rates imply that 3 cm-diameter spherical glomerocrysts could have grown in as little as 7–23 days, consistent with the short residence timescales calculated (Figs. 3, 4, 5) and well within the eruption timescale of the GTFE (Fedotov et al., 1980a,b). We conclude that these short timescales and rapid growth conditions imply that radially oriented plagioclase glomerocrysts record syn-eruptive magmatic processes.

5.2. Plagioclase: a monitor of short-term volatile-fluxing?

The concentrations of major and trace elements, both compatible and incompatible, in plagioclase remain relatively constant (Fig. 2, electronic appendix Fig. S3). The near-constancy of major and trace elements during growth is consistent with crystallization in a melt-dominated environment whereby crystal growth results in little change in melt fraction. Conversely, melt inclusions in plagioclase show significant H_2O variations (<0.1–0.9 wt% H_2O; Fig. 6a), and CO_2 abundances increase as H_2O abundances decrease (Fig. 6b). This inverse correlation between CO_2 and H_2O abundances is unlike equilibrium, closed-system degassing, which should lead to rapid loss of CO_2 and near-constant H_2O as a con-

sequence of the lower solubility of CO_2 in the melt (e.g., Papale, 2005).

Two distinct processes could lead to shifts to lower H_2O at constant or increasing CO_2, namely disequilibrium degassing and CO_2-fluxing. The lower diffusivity of CO_2 compared to H_2O implies that in dynamic subvolcanic systems, disequilibrium degassing could result in melt inclusions losing H_2O whilst retaining elevated concentrations of CO_2, as shown experimentally by Pichavant et al. (2013). This is a process especially likely to occur in shallow volcanic systems affected by rapid, decompression-driven crystallization. By combining high-resolution CO_2 and H_2O analysis of melt inclusions and numerical modelling of magma degassing upon ascent, Yoshimura (2015) showed how CO_2/H_2O might indeed shift to higher values as a result of such a kinetic effect. However, Yoshimura (2015) illustrated that such kinetic effects are strongly dependant on ascent rates, with significant shifts towards high CO_2/H_2O ratios requiring abnormally high ascent rates (>1000 m/s). Thus, although such kinetic effects are likely to occur, Tolbachik melt inclusions reach a maximum of 1200 ppm CO_2 at <800 ppm H_2O, suggesting an alternative mechanism is likely.

This second mechanism, CO_2-fluxing, is likely to result from competing CO_2-H_2O solubility in a volatile-saturated system, where the addition of CO_2 will lead to a decrease in the solubility of H_2O (e.g. Caricchi et al., 2018). Melt inclusion data from diverse volcanic systems has shown that significant shifts in CO_2/H_2O can result from CO_2 being added to the system as a gas fluxing through the magmatic reservoir en route to the surface, either during or between eruptions (Métrich et al., 2010; Blundy et al., 2010; Yoshimura, 2015; Caricchi et al., 2018). Loss of CO_2 from deep magmatic reservoirs allows for pulses of CO_2-rich fluid to rise through the crust, interacting with shallow magmatic reservoirs and shifting melt compositions towards H_2O-poor, CO_2-rich compositions (Blundy et al., 2010; Caricchi et al., 2018). Such conditions are likely at Tolbachik, where pre-1972, CO_2–rich magmas (500–1000 ppm CO_2) have been identified (Kamenetsky et al., 2017).

As the composition and stability of plagioclase is very sensitive to variations in melt composition and P-T conditions (e.g. Feig et al., 2006), zoning patterns are traditionally ascribed to rejuvenation by hotter mafic magmas, melt differentiation or crystallization kinetics (Singer et al., 1995; L'Heureux and Fowler, 1996; Stewart and Fowler, 2001). However, the growth of glomerocrysts in a dynamic, melt-rich environment with melt inclusions of similar composition throughout the glomerocryst precludes such processes (Fig. 2). An alternative explanation, consistent with our observations, is that crystallization and resorption of plagioclase and olivine is controlled by the rhythmic interplay of H_2O and CO_2 abundances serving to alternately suppress and elevate liquidus temperature, respectively, so driving undercooling and superheating of the magma at roughly constant temperature. Rhyolite-MELTS (Gualda et al., 2012) modelling indicates that a shift from $XH_2O = 1$ to $XCO_2 = 1$ at 5–20 MPa captures the overall range of observed plagioclase composition (Fig. 6c). Intermittent resorption zones in plagioclase are rimmed by higher-An contents reaching An_{70} whereas mm-wide segments dominated by oscillatory zoning vary primarily between An_{55} and An_{65}. Thus, one mechanism allowing for both oscillatory zoning and the antithetic variation in CO_2 and H_2O abundances is interplay between CO_2-rich and H_2O-rich gases fluxing the system. Increasing H_2O in the system will lead to more calcic plagioclase and, at elevated H_2O abundances, resorption as a result of the sensitivity of plagioclase stability to increasing H_2O abundance (e.g. Feig et al., 2006). Such resorption textures followed by an increase in X_{An} are common in plagioclase glomerocrysts of the GTFE (Figs. 1 and 3b). Conversely, H_2O loss as a consequence of CO_2-fluxing will lead to undercooling and rapid crystallization of plagioclase (oversaturation) with more sodic compositions.

Due to variation in H_2O and CO_2 solubility in silicate melts as a function of pressure (e.g. Ghiorso and Gualda, 2015), degassing of magmas at variable depths in intracrustal magmatic systems (e.g. Cashman et al., 2017) can lead to release of both CO_2 and H_2O-rich gases. Pulses of high-pressure CO_2-bearing gas waves will expel H_2O out of shallower stored magmatic reservoirs, thereby creating a compositionally and temporally heterogeneous gas column beneath the volcano. In this way, competition between CO_2-rich and H_2O-rich gases fluxing shallow volcanic reservoirs can control the textures, compositions and growth rates of plagioclase glomerocrysts. Rapid growth of plagioclase glomerocrysts as a consequence of volatile-fluxing during the more explosive stages of the GTFE is consistent with strombolian explosive activity being controlled by an important gas-component fluxing the system from below (e.g. Chouet et al., 1974; Kondo et al., 2019).

Experimental investigations into plagioclase crystallization suggest that higher growth rates (Shea and Hammer, 2013) occur at an undercooling (ΔT) on the order of 50-100 °C, whereas alkali-feldspar glomerocrysts crystallizing from initially superheated melts show higher growth rates at lower ΔT of ca 40 °C. At 5 to 20 MPa (Arzilli and Carroll, 2013). Rhyolite-MELTS indicates that the saturation temperature of plagioclase in Tolbachik melts is increased by 30–65 °C when driving the melt from H_2O-saturated to CO_2-saturated conditions (Fig. 6). This ΔT of 30–65 °C is equivalent to the loss of ca. 0.5–1 wt% H_2O at constant pressure, consistent with the observed fluctuations of volatiles in our melt inclusions (Fig. 6). CL imaging of plagioclase crystals indicates that oscillatory-zoning patterns are <10 to 180 µm wide (Fig. 1 and electronic appendix Figs. S1, S2). Within these zones, plagioclase composition varies on the order of <5 An, interspersed with occasionally larger variations of 5-10 An. Although we cannot fully discount boundary layer effects in the formation of such rhythmic oscillatory zoning patterns (e.g. L'Heureux and Fowler, 1996), the dynamic as well as melt- and volatile-rich conditions of the Tolbachik magmatic system suggest that boundary layers would likely be unstable. In addition, the 10-100 micron-scale growth and resorption zones of plagioclase (Fig. 1, electronic appendix Fig. S1) imply that these minerals were alternately growing and dissolving on short timescales. Pulses of plagioclase growth over a <10 to 100 µm due to loss of H_2O would have been short prior to the cessation of growth or initiation of resorption. Consequently, an alternative interpretation is that oscillatory layering reflects CO_2- and H_2O-fluxing through the volcanic conduit on the order of minutes to hours, assuming previously discussed high crystal growth rates.

5.3. H_2O and CO_2-fluxing as a control on strombolian eruptions?

The mechanisms involved in the formation of Tolbachik glomerocrysts are illustrated schematically in Fig. 7. Formation of new scoria cones during strombolian and effusive volcanic activity during the initial months of the GTFE were generally preceded by ground deformation and an increase in recorded volcanic tremors down to 10-20 km depth within 2 weeks prior to eruption (Fedotov et al., 1980a,b). Such timescales of seismic activity followed by eruption, lava discharge and rapid decrease in seismic activity are consistent with the growth rates and residence timescales inferred from plagioclase and olivine, suggesting that Tolbachik plagioclase glomerocrysts formed in a dynamic, melt-rich environment as a response to pre- to syn-eruptive fluctuations in volatile abundances.

The fact that CO_2-H_2O in melt inclusions do not track simple isobars (Fig. 6), as would be expected for fluid-melt interactions at fixed pressure, imply that addition of CO_2 on the order of 60 ppm

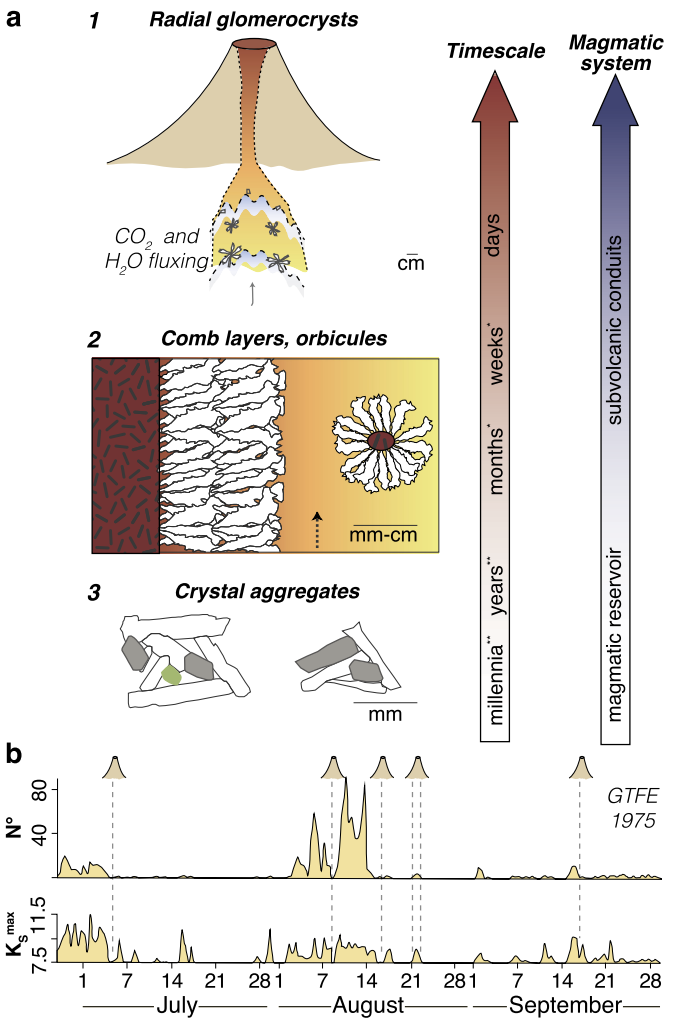

Fig. 7. (a) Radial plagioclase glomerocrysts (1) together with comb layers and orbicules (2) represent subvolcanic conduit processes, whereas more traditional types of crystal aggregates reflect magmatic reservoir systems (3); * = Timescales inferred from McCarthy and Müntener (2016) and Antonelli et al. (2019). ** = Longer residence timescales are represented by more traditional types of crystal aggregates that likely reflect remobilized crystal mush fragments (e.g. Cashman et al., 2017); (b) Recorded seismic activity from July to September 1975 during the Great Tolbachik Fissure Eruption (GTFE). Top graph represents the daily number of earthquakes with Magnitude ≥ 2. The lower graph represents the maximum energy class of earthquakes (Ks^{max}) determined from short-period S waves. Formation of eruptive vents is illustrated with small cone symbols (modified from Fedotov et al., 1980a,b).

leads to pressure variations between 5 and 15 MPa (Fig. 6). Overpressure of magmatic reservoirs to exceed the tensile strength of overlying rocks is an essential mechanism to trigger and drive volcanic eruptions and is generally proposed to be related to magmatic rejuvenation, passive degassing or second boiling through crystallisation (e.g. Tait et al., 1989; Jellinek and DePaolo, 2003; Gudmundsson, 2012).

In the case of strombolian activity, the ascent of gas pulses or waves of gas layers control the rhythmicity of eruption dynamics (e.g. Chouet et al., 1974; Kondo et al., 2019). As recorded by plagioclase zoning and melt inclusions, CO_2-fluxing on hourly timescales might have a significant impact on the confining pressure of the small and shallow magmatic reservoirs beneath Tolbachik, within the range of over-pressure triggering volcanic eruptions (Tait et al., 1989; Jellinek and DePaolo, 2003). Fluxing of CO_2, and concomitant displacement of H_2O from solution, induces an increase in the volume of the magmatic reservoir that can trigger volcanic unrest (Caricchi et al., 2018), especially for melt-rich systems and short-term fluxing. Such conditions are consistent with shallow earthquake swarms and ground deformation on the weeks prior to the formation of scoria cones during the GTFE (Fedotov et al., 1980b) as well as with cyclical ground deformation contemporaneous with explosive strombolian eruptions (e.g. Kondo et al., 2019 and references therein).

Hence, extensive oscillatory zoning of radial plagioclase glomerocrysts interspersed with high-anorthite resorption zones can be used as archives of rhythmic pressure fluctuations of shallow subvolcanic reservoirs feeding strombolian explosive activity driven by short-term CO_2– and H_2O–fluxing through a compositionally heterogeneous gas column.

5.4. Glomerocrysts and orbicular rocks: the plutonic and volcanic connection

Decompression-driven crystallization leading to the growth of plagioclase glomerocrysts may be a ubiquitous phenomenon in (sub)volcanic systems. Magmatic layering found in arc-related, subvolcanic settings show similar crystallization conditions to Tolbachik plagioclase glomerocrysts, namely comb layers and orbicular rocks (e.g. Moore and Lockwood, 1973) (Figs. 7, 8). This type of igneous layering is characterized by elongated plagioclase crystals forming plagioclase crescumulates on pluton walls (Fig. 8a, b) and around rock fragments (Fig. 8c, d). Comb layers and orbicular rocks are generally found along 100s m-wide zones at the rims of otherwise homogenous plutons (e.g. Moore and Lockwood, 1973). The combination of a cumulate signature for each crescumulate layer implying the loss of residual melt upon crystallization (McCarthy and Müntener, 2017), the predominance of plagioclase as the initial and main crystallizing phase (Moore and Lockwood, 1973; McCarthy and Müntener, 2017), and the lack of significant mineralogical or compositional evolution of minerals over tens to hundreds of comb layers (McCarthy and Müntener, 2016, 2017) implies that comb layers and orbicules, like Tolbachik glomerocrysts, form in dynamic, subvertical conduits in melt- and volatile-rich conditions (Moore and Lockwood, 1973, McCarthy and Müntener, 2016, 2017) (Fig. 6). Such dynamic conditions are also consistent with magmatic breccias, as well as remobilized fragments of pre-existing comb layers and orbicular rocks upon which new generations of crescumulates form (Moore and Lockwood, 1973). As at Tolbachik, orbicular rocks grow in near-isothermal conditions ≥950-1000 °C (McCarthy and Müntener, 2016, 2017), requiring an additional mechanism (gas fluxing) to promote crystal growth (and resorption; Arzilli et al., 2015, McCarthy and Müntener, 2016, 2017). Estimated timescales of growth of comb layers and orbicular rocks based on comparison with experimental datasets and kinetic fractionation of Calcium isotopes in plagioclase indicate timescales of weeks to months (McCarthy and Müntener, 2016; Antonelli et al., 2019). Such timescales are thus similar to those recorded in Tolbachik glomerocrysts.

The comparable mineral textures and growth mechanisms imply a similar origin for both subvolcanic (comb layers, orbicular rocks) and volcanic (glomerocrysts) magmatic lithologies (Fig. 7a). While long timescales and slow cooling in magma chambers or large reservoirs are the more commonly invoked mechanisms responsible for magmatic layering (e.g., Wager and Brown, 1967) our data rather support the conclusion that comb layering, orbicular rocks and volcanic glomerocrysts are a rapid growth phenomena. Thus, vertical, radial magmatic layering dominated by elongated plagioclase offers new avenues for understanding the dynamics of shallow, dynamic melt extraction zones in terms of rapidly fluctuating P-T-H_2O-CO_2 conditions within sub-volcanic systems on eruptive timescales.

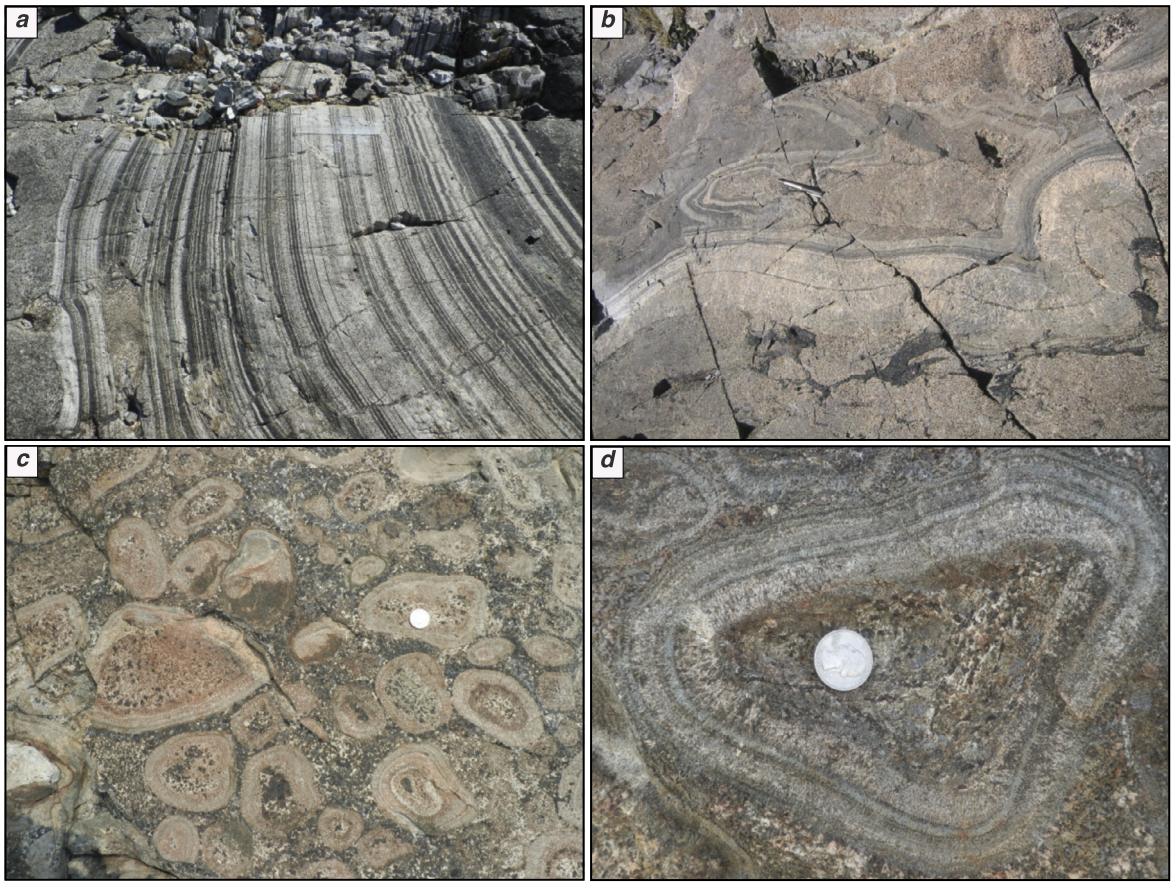

Fig. 8. (a, b) Examples of plagioclase-dominated crescumulates growing on pluton walls (comb layering) from (a) the granodiorite Pyramid pluton (Volcanic Lakes, central Sierra Nevada) (scale is a 30 cm long ruler); (b) from the north flank of Cornone de Blumone, Adamello intrusive complex (northern Italy). Note pegmatitic amphibole-gabbro patch in upper right of photo. In both (a) and (b) white crystals growing perpendicular to the layering are plagioclase; black crystals are predominantly amphibole; (c, d) radially oriented plagioclase-crescumulates growing on gabbro xenoliths forming orbicules from (c) the Fisher Lake pluton (Northern Sierra Nevada, California), and (d) from the San Marcos gabbro (Pine Valley, Southern California); the interstitial reddish mineral associated with radial plagioclase is orthopyroxene whereas amphibole (in black) is generally found in the matrix (e.g. Moore and Lockwood, 1973; McCarthy and Müntener, 2017).

6. Conclusions

Mineral aggregates are generally thought to represent the remobilization of variably long-lived, crystal-bearing magmatic reservoirs. Based on mineral aggregates from the Great Tolbachik Fissure Eruption of 1975-1976, we show that cm-wide, radially-oriented plagioclase glomerocrysts can form on short, eruptive timescales. As a consequence, radial plagioclase records short-term processes, such as pre-to syn-eruptive CO_2- and H_2O-fluxing in melt-rich (sub)volcanic conduits. Such short-term CO_2-fluxing, as reflected in both melt inclusion data and in the compositional variations in plagioclase, may control the dynamics of volcanic eruptions by generating significant overpressure. Volcanic plagioclase might, therefore, offer a novel way of targeting transient processes of volatile migration in modern and ancient arc systems and their role as eruption triggers. Additionally, plagioclase comb layering and orbicular rocks showing similar growth conditions as plagioclase glomerocrysts, imply that certain types of vertical, plutonic layering might form on volcanic timescales.

CRediT authorship contribution statement

A.Mc. and J.B. designed the research. P.V. performed SEM, EBSD and Cathodoluminescence. A.Mc., A.Me, and S.E. performed nano-SIMS analysis. A.Mc. performed SIMS and Microprobe analysis. C.C-M. performed the diffusion modeling. A.Mc. wrote the manuscript with input from C.C-M., J.B., and P.V.

Declaration of competing interest

The authors declare that they have no known competing financial interests or personal relationships that could have appeared to influence the work reported in this paper.

Acknowledgements

We are grateful for the dedicated support from the NERC ion-microprobe facility at Edinburgh University, Y. Guan and E. Stolper at Caltech, and B. Buse and S. Kearns for help on the Bristol electron microprobe; A.McC. and C.C.-M. acknowledge the support of SNSF grants P2LAP2_171819 and P2GEP2_165116 respectively. J.B. acknowledges the support of NERC funding (NE/P017371/1). One anonymous reviewer and F. Arzilli, as well as additional comments and editorial handling by H. Handley, helped to improve the paper and are gratefully acknowledged.

Appendix A. Supplementary material

Supplementary material related to this article can be found online at https://doi.org/10.1016/j.epsl.2020.116596.

References

Annen, C., Blundy, J.D., Sparks, R.S.J., 2006. The genesis of intermediate and silicic magmas in deep crustal hot zones. J. Petrol. 47, 505–539. https://doi.org/10.1093/petrology/egi084.

Antonelli, M.A., Mittal, T., McCarthy, A., Tripoli, B., Watkins, J.M., DePaolo, D.J., 2019. Ca isotopes record rapid crystal growth in volcanic and subvolcanic systems. Proc. Natl. Acad. Sci. 116 (41), 20315–20321. https://doi.org/10.1073/pnas.1908921116.

Arzilli, F., Carroll, M.R., 2013. Crystallization kinetics of alkali feldspars in cooling and decompression-induced crystallization experiments in trachytic melt. Contrib. Mineral. Petrol. 166 (4), 1011–1027. https://doi.org/10.1007/s00410-013-0906-1.

Arzilli, F., Mancini, L., Voltolini, M., Cicconi, M.R., Mohammadi, S., Giuli, G., Mainprice, D., Paris, E., Barou, F., Carroll, M.R., 2015. Near-liquidus growth of feldspar spherulites in trachytic melts: 3D morphologies and implications in crystallization mechanisms. Lithos 216, 93–105. https://doi.org/10.1016/j.lithos.2014.12.003.

Batanova, V.G., Thompson, J.M., Danyushevsky, L.V., Portnyagin, M.V., Garbe-Schönberg, D., Hauri, E., Kimura, J.I., Chang, Q., Senda, R., Goemann, K., Chauvel, C., 2019. New olivine reference material for in situ microanalysis. Geostand. Geoanal. Res. 43 (3), 453–473. https://doi.org/10.1111/ggr.12266.

Blundy, J.D., Cashman, K.V., 2005. Rapid decompression-driven crystallization recorded by melt inclusions from Mount St. Helens volcano. Geology 33, 793–796. https://doi.org/10.1130/G21668.1.

Blundy, J.D., Cashman, K.V., Rust, A.C., Witham, F., 2010. A case for CO2-rich arc magmas. Earth Planet. Sci. Lett. 290, 289–301. https://doi.org/10.1016/j.epsl.2009.12.013.

Bouvet de Maisonneuve, C., Dungan, M.A., Bachmann, O., Burgisser, A., 2013. Petrological insights into shifts in eruptive styles at Volcán Llaima (Chile). J. Petrol. 54, 393–420. https://doi.org/10.1093/petrology/egs073.

Caricchi, L., Sheldrake, T.E., Blundy, J.D., 2018. Modulation of magmatic processes by CO2 flushing. Earth Planet. Sci. Lett. 491, 160–171. https://doi.org/10.1016/j.epsl.2018.03.042.

Cashman, K.V., Sparks, R.S.J., Blundy, J.D., 2017. Vertically extensive and unstable magmatic systems: a unified view of igneous processes. Science 355, eaag3055. https://doi.org/10.1126/science.aag3055.

Cherniak, D.J., Watson, E.B., 1994. A study of strontium diffusion in plagioclase using Rutherford backscattering spectroscopy. Geochim. Cosmochim. Acta 58, 5179–5190. https://doi.org/10.1016/0016-7037(94)90303-4.

Chouet, B., 1996. Long-period volcano seismicity: its source and use in eruption forecasting. Nature 380, 309–316. https://doi.org/10.1038/380309a0.

Chouet, B., Hamisevicz, N., McGetchin, T.R., 1974. Photoballistics of volcanic jet activity at Stromboli, Italy. J. Geophys. Res. 79 (32), 4691–4976. https://doi.org/10.1029/JB079i032p04961.

Churikova, T.G., Gordeychik, B.N., Edwards, B.R., Ponomareva, V.V., Zelenin, E.A., 2015. The Tolbachik volcanic massif: a review of the petrology, volcanology and eruption history prior to the 2012–2013 eruption. J. Volcanol. Geotherm. Res. 307, 3–21. https://doi.org/10.1016/j.jvolgeores.2015.10.016.

Costa, F., Dohmen, R., Chakraborty, S., 2008. Timescales of magmatic processes from modeling the zoning patterns of crystals. Rev. Mineral. Geochem. 69, 545–594. https://doi.org/10.2138/rmg.2008.69.14.

Dohmen, R., Blundy, J.D., 2014. A predictive thermodynamic model for element partitioning between plagioclase and melt as a function of pressure, temperature and composition. Am. J. Sci. 314, 1319–1372. https://doi.org/10.2475/09.2014.04.

Dohmen, R., Faak, K., Blundy, J.D., 2017. Chronometry and speedometry of magmatic processes using chemical diffusion in olivine, plagioclase and pyroxenes. Rev. Mineral. Geochem. 83, 535–575. https://doi.org/10.2138/rmg.2017.83.16.

Fedotov, S.A., Chirkov, A.M., Gusev, N.A., Kovalev, G.N., Slezin, Y.B., 1980a. The large fissure eruption in the region of Plosky Tolbachik volcano in Kamchatka, 1975–1976. Bull. Volcanol. 43 (1), 47–60.

Fedotov, S.A., Gorelchik, V.I., Stepanov, V.V., 1980b. Seismological studies on the mechanism of the large Tolbachik fissure eruption, 1975–1976. Bull. Volcanol. 43, 73–84.

Feig, S.T., Koepke, J., Snow, J.E., 2006. Effect of water on tholeiitic basalt phase equilibria: an experimental study under oxidizing conditions. Contrib. Mineral. Petrol. 152, 611–638. https://doi.org/10.1007/s00410-006-0123-2.

Ghiorso, M.S., Gualda, G.A.R., 2015. An H2O–CO2 mixed fluid saturation model compatible with rhyolite-MELTS. Contrib. Mineral. Petrol. 169, 1–30. https://doi.org/10.1007/s00410-015-1141-8.

Giletti, B.J., Casserly, J.E.D., 1994. Strontium diffusion kinetics in plagioclase feldspars. Geochim. Cosmochim. Acta 58, 3785–3793. https://doi.org/10.1016/0016-7037(94)90363-8.

Gualda, G.A.R., Ghiorso, M.S., Lemons, R.V., Carley, T.L., 2012. Rhyolite-MELTS: a modified calibration of MELTS optimized for silica-rich, fluid-bearing magmatic systems. J. Petrol. 53, 875–890. https://doi.org/10.1093/petrology/egr080.

Gudmundsson, A., 2012. Magma chambers: formation, local stresses, excess pressures, and compartments. J. Volcanol. Geotherm. Res. 237, 19–41. https://doi.org/10.1016/j.jvolgeores.2012.05.015.

Jellinek, A.M., DePaolo, D.J., 2003. A model for the origin of large silicic magma chambers: precursors of caldera-forming eruptions. Bull. Volcanol. 65, 363–381. https://doi.org/10.1007/s00445-003-0277-y.

Kamenetsky, V.S., Zelenski, M., Gurenko, A., Portnyagin, M., Ehrig, K., Kamenetsky, M., Churikova, T., Feig, S., 2017. Silicate-sulfide liquid immiscibility in modern arc basalt (Tolbachik volcano, Kamchatka): part II. Composition, liquidus assemblage and fractionation of the silicate melt. Chem. Geol. 471, 92–110. https://doi.org/10.1016/j.chemgeo.2017.09.019.

Kondo, G., Aoyama, H., Nishimura, T., Ripepe, M., Lacanna, G., Genco, R., Kawaguchi, R., Yamada, T., Miwa, T., Fujita, E., 2019. Gas flux cyclic regime at an open vent magmatic column inferred from seismic and acoustic records. Sci. Rep. 9 (1), 1–8. https://doi.org/10.1038/s41598-019-42033-z.

L'Heureux, I., Fowler, A.D., 1996. Isothermal constitutive undercooling as a model for oscillatory zoning in plagioclase. Can. Mineral. 34, 1137–1147.

Lofgren, G.E., Donaldson, C.H., 1975. Curved branching crystals and differentiation in comb-layered rocks. Contrib. Mineral. Petrol. 49, 309–319. https://doi.org/10.1007/BF00376183.

McCarthy, A., Müntener, O., 2016. Comb layering monitors decompressing and fractionating hydrous mafic magmas in subvolcanic plumbing systems (Fisher Lake, Sierra Nevada, USA). J. Geophys. Res., Solid Earth 121, 8595–8621. https://doi.org/10.1002/2016JB013489.

McCarthy, A., Müntener, O., 2017. Mineral growth in melt conduits as a mechanism for igneous layering in shallow arc plutons: mineral chemistry of Fisher Lake orbicules and comb layers (Sierra Nevada, USA). Contrib. Mineral. Petrol. 172, 55. https://doi.org/10.1007/s00410-017-1371-z.

Métrich, N., Bertagnini, A., Di Muro, A., 2010. Conditions of magma storage, degassing and ascent at Stromboli: new insights into the volcano plumbing system with inferences on the eruptive dynamics. J. Petrol. 51, 603–626. https://doi.org/10.1093/petrology/egp083.

Milman-Barris, M.S., Beckett, J.R., Baker, M.B., Hofmann, A.E., Morgan, Z., Crowley, M.R., Vielzeuf, D., Stolper, E., 2008. Zoning of phosphorus in igneous olivine. Contrib. Mineral. Petrol. 155, 739–765. https://doi.org/10.1007/s00410-007-0268-7.

Moore, J.G., Lockwood, J.P., 1973. Origin of comb layering and orbicular structure, Sierra Nevada batholith, California. Geol. Soc. Am. Bull. 84, 1–20. https://doi.org/10.1130/0016-7606(1973)84<1:OOCLAO>2.0.CO;2.

Mourey, A.J., Shea, T., 2019. Forming olivine phenocrysts in basalt: a 3D characterization of growth rates in laboratory experiments. Front. Earth Sci. 7, 300. https://doi.org/10.3389/feart.2019.00300.

Newman, S., Lowenstern, J.B., 2002. VolatileCalc: a silicate melt–H2O–CO2 solution model written in Visual Basic for excel. Comput. Geosci. 28, 597–604. https://doi.org/10.1016/S0098-3004(01)00081-4.

Papale, P., 2005. Determination of total H_2O and CO_2 budgets in evolving magmas from melt inclusion data. J. Geophys. Res. 110, B03208. https://doi.org/10.1029/2004JB003033.

Pichavant, M., Di Carlo, I., Rotolo, S.G., Scaillet, B., Burgisser, A., Le Gall, N., Martel, C., 2013. Generation of CO2-rich melts during basalt magma ascent and degassing. Contrib. Mineral. Petrol. 166, 545–561. https://doi.org/10.1007/s00410-013-0890-5.

Punin, Y.O., Shtukenberg, A.G., Smetannikova, O.G., Amelin, K.S., 2010. Plagioclase twin associations from the basic volcanic rocks of the Kamchatka, Russia: growth conditions and formation mechanisms. Eur. J. Mineral. 22, 139–145. https://doi.org/10.1127/0935-1221/2009/0021-1979.

Shapiro, N.M., Droznin, D.V., Droznina, S.Ya., Senyukov, S.L., Gusey, A.A., Gordeev, E.I., 2017. Deep and shallow long-period volcanic seismicity linked by fluid-pressure transfer. Nat. Geosci. 10, 442–445. https://doi.org/10.1038/ngeo2952.

Shea, T., Hammer, J.E., 2013. Kinetics of cooling- and decompression-induced crystallization in hydrous mafic-intermediate magmas. J. Volcanol. Geotherm. Res. 260, 127–145. https://doi.org/10.1016/j.jvolgeores.2013.04.018.

Singer, B.S., Dungan, M.A., Layne, G.D., 1995. Textures and Sr, Ba, Mg, Fe, K, and Ti compositional profiles in volcanic plagioclase: clues to the dynamics of calc-alkaline magma chambers. Am. Mineral. 80, 776–798. https://doi.org/10.2138/am-1995-7-815.

Sisson, T.W., Grove, T.L., 1993. Temperatures and H_2O contents of low-MgO high-alumina basalts. Contrib. Mineral. Petrol. 113, 167–184. https://doi.org/10.1007/BF00283226.

Sparks, R.S.J., Sigurdsson, H., Wilson, L., 1977. Magma mixing: a mechanism for triggering acid explosive eruptions. Nature 267, 315–318. https://doi.org/10.1038/267315a0.

Stewart, M.L., Fowler, A.D., 2001. The nature and occurrence of discrete zoning in plagioclase from recently erupted andesitic volcanic rocks, Montserrat. J. Volcanol. Geotherm. Res. 106, 243–253. https://doi.org/10.1016/S0377-0273(00)00240-7.

Tait, S., Jaupart, C., Vergniolle, S., 1989. Pressure, gas content and eruption periodicity of a shallow, crystallising magma chamber. Earth Planet. Sci. Lett. 92, 107–123. https://doi.org/10.1016/0012-821X(89)90025-3.

Wager, L.R., Brown, G.M., 1967. Layered Igneous Rocks. WH Freeman.

Watson, E.B., Cherniak, D.J., Holycross, M.E., 2015. Diffusion of phosphorus in olivine and molten basalt. Am. Mineral. 100, 2053–2065. https://doi.org/10.2138/am-2015-5416.

Woods, A.W., Cardoso, S.S., 1997. Triggering basaltic volcanic eruptions by bubble-melt separation. Nature 385 (6616), 518–520. https://doi.org/10.1038/385518a0.

Yoshimura, S., 2015. Diffusive fractionation of H_2O and CO_2 during magma degassing. Chem. Geol. 411, 172–181. https://doi.org/10.1016/j.chemgeo.2015.07.003.